Magnetization reversal driven by electron localization-delocalization crossover in the inverse spinel Co_2VO_4

Abhijit Bhat Kademane [1,*,†] Churna Bhandari [2,*,‡] Durga Paudyal [2,3] Stephen Cottrell,[4] Pinaki Das,[2] Yong Liu [2]
Yuen Yiu,[2] C. M. Naveen Kumar [5,6] Konrad Siemensmeyer [7] Andreas Hoser,[7] Diana Lucia Quintero-Castro,[1]
David Vaknin [2,8] and Rasmus Toft-Petersen [9,10,§]

[1]*Department of Mathematics and Physics, Universitetet i Stavanger, 4036 Stavanger, Norway*
[2]*Ames Laboratory, Iowa State University, Ames, Iowa 50011, USA*
[3]*Department of Electrical and Computer Engineering, Iowa State University, Ames, Iowa 50011, USA*
[4]*ISIS Facility, STFC Rutherford Appleton Laboratory, Harwell Science and Innovation Campus,
Chilton, Didcot, Oxon OX11 0QX, United Kingdom*
[5]*Institute of Solid State Physics, Vienna University of Technology, Wiedner Hauptstrae 810, 1040 Vienna, Austria*
[6]*AGH University of Science and Technology, Faculty of Physics and Applied Computer Science, 30-059 Kraków, Poland*
[7]*Helmholtz Zentrum Berlin für Materialien und Energie, D-14109 Berlin, Germany*
[8]*Department of Physics and Astronomy, Iowa State University, Ames, Iowa 50011, USA*
[9]*Department of Physics, Technical University of Denmark, DK-2800 Kongens Lyngby, Denmark*
[10]*European Spallation Source, Partikelgatan 2, 224 84 Lund, Sweden*

Neutron diffraction, magnetization, and muon spin relaxation measurements, supplemented by density functional theory (DFT) calculations are employed to unravel temperature-driven magnetization reversal in inverse spinel Co_2VO_4. All measurements show a second-order magnetic phase transition at $T_C = 168$ K to a collinear ferrimagnetic phase. Neutron diffraction measurements reveal two antiparallel ferromagnetic (FM) sublattices, belonging to magnetic ions on two distinct crystal lattice sites, where the relative balance between the two sublattices determine the net FM moment in the unit cell. As the evolution of the ordered moment with temperature differs between the two sublattices, the net magnetic moment reaches a maximum at $T_{NC} = 138$ K and reverses its sign at $T_{MR} = 65$ K. The DFT results suggest that the underlying microscopic mechanism for the reversal is a delocalization of the unfilled $3d$-shell electrons on one sublattice just below T_C, followed by a gradual localization as the temperature is lowered. This delocalized-localized crossover is supported by muon spectroscopy results, as strong T_1 relaxation observed below T_C indicates fluctuating internal fields.

I. INTRODUCTION

AB_2X_4-type spinel compounds, with tetrahedral A sites and octahedral B sites, have been an anchoring point for some of the earliest work on magnetism that led to the seminal Néel [1] and Yafet-Kittel [2] models. The spinel (and the inverse-spinel) compounds display a complex interplay among lattice, spin, charge, and orbital degrees of freedom [3], where intriguing phenomena emerge [4,5]. Indeed, interest in these systems persists, as they exhibit exotic magnetic phenomena, such as multiferroic effects and the spin-liquid state that result from spin-orbit coupling and geometric frustration associated with the pyrochlore sublattice of the B site [6,7].

Magnetization reversal (MR) is a crossover phenomenon, where the interplay of the ordering of two or more antiparallel magnetic sublattices results in spontaneous reversal of bulk magnetization [8–10]. Additionally, the MR phenomenon can also occur due to an imbalance of spin and orbital moments. Néel [1] provided a phenomenological mean-field theory to explain the interplay of two antiparallel ferromagnetic (FM) sublattices in some ferrimagnetic systems. Subsequently, Belov [11,12] proposed the role of delocalized electrons acting as a weak magneto-electronic sublattice as a driving mechanism for compensation phenomena in magnetite.

A prototypical class of spinel compounds is the vanadate of type AV_2O_4 and its inverse-spinel counterpart A_2VO_4. At high temperatures, these systems form a cubic structure with space group $Fd\bar{3}m$. For AV_2O_4 with a nonmagnetic transition metal ion, such as Mg^{2+} or Zn^{2+}, in the A site, a cubic-to-tetragonal phase transition accompanied by an antiferromagnetic (AFM) phase has been reported [13,14]. On the other hand, magnetic ions on the A site, such as in MnV_2O_4, FeV_2O_4, or CoV_2O_4, show a multitude of structural and magnetic transitions by virtue of coupled spin and orbital degrees of freedom [15–19]. Specifically, for CoV_2O_4, orbital glasslike behavior has been reported [20,21] and *spin-ice rules* have been outlined in studies of MnV_2O_4 and FeV_2O_4 [15,16]. Additionally, CoV_2O_4 is

———————
*These authors contributed equally to this work.
†abhijit.bhatkademane@uis.no
‡cbb@ameslab.gov
§rasp@fysik.dtu.dk

known to sit on the edge of the itinerant electron limit [22]. The inverse-spinel vanadate counterparts (of type A_2VO_4), which are more complex due to random cation distribution, have yet to be thoroughly explored. Indeed, the intriguing MR phenomenon was observed in inverse spinel Co_2VO_4 [8]. It has been proposed that the cation distribution of Co_2VO_4 is $Co_A^{2+}(Co^{2+}V^{4+})_B O_4^{2-}$ [8,23], which has been subsequently confirmed by x-ray photoelectron spectroscopy measurements in Ref. [24]. Additionally, magnetic interaction mechanisms in Co_2VO_4 have been proposed using semi-empirical rules for magnetic interactions in spinels [8,25]. While temperature-driven MR for Co_2VO_4 and Co_2TiO_4 has been experimentally explored [8,26–28], the fundamental driving mechanism behind MR in the inverse spinels remains to be understood.

Here, we examine the temperature evolution of magnetic structures using neutron diffraction, magnetization, polarized muon spectroscopy, and electronic structure calculations of Co_2VO_4. We establish multiple phase transitions in the magnetically ordered phase as well as temperature-driven MR. Neutron diffraction reveals the structure to be composed of two nearly balanced antiparallel FM sublattices, on the A and B sites, giving rise to a net ferrimagnetic phase that evolves with temperature. A significant difference between the temperature evolution of the ordered moment of the two sublattices causes a tipping of this balance, giving rise to a change in sign of the net magnetic moment in the unit cell.

To shed light on the underlying causes of such a tipping of the ferrimagnetic balance, we performed density functional theory (DFT) calculations, with *delocalized* calculation addressing the high-temperature region, and *localized* calculation for low temperatures. The DFT results are shown to be consistent with MR. Using muon spectroscopy, dynamic T_1 relaxation is observed in an extended temperature interval just below T_C, indicative of magnetic moment fluctuations at high temperatures. These fluctuations support our interpretation of a gradual crossover between delocalization and localization of electrons as the underlying microscopic mechanism for the MR.

II. EXPERIMENTAL AND COMPUTATIONAL DETAILS

The polycrystalline sample of Co_2VO_4 was prepared using a solid-state reaction as described in Ref. [29]. The x-ray diffraction (XRD) measurement confirms the formation of Co_2VO_4 spinel. Rietveld refinement of neutron diffraction and XRD data (at 300 K) confirm the cubic $Fd\bar{3}m$ symmetry. Due to A/B site inversion ($A = 8b$ tetrahedral and $B = 16c$ octahedral) the formal chemical formula of Co_2VO_4 is $Co_\nu^{2+}V_{1-\nu}^{4+}[V_\nu^{4+}Co_{2-\nu}^{2+}]O_4$, where ν is the inversion parameter, and the B site cations are enclosed in brackets. The refinement yields that the degree of inversion $\nu \simeq 1$, i.e., the actual $Co_A^{2+}[V^{4+}Co^{2+}]_B O_4$, where Co^{2+} occupies the A site and the remaining Co^{2+} and V^{4+} are distributed evenly in the B site. Two impurity phases are identified. Peaks at 2.66 and 3.03 Å^{-1} correspond to the $Co_3V_2O_8$ phase [30], while peaks at 2.56 and 2.94 Å^{-1} corresponds to CoO structural phase. Additionally, at $T_N \simeq 290$ K, the CoO impurity phase orders into an AFM state that is incommensurate with its crystal structure corresponding to propagation vector $k = (\frac{1}{2}, \frac{1}{2}, \frac{1}{2})$

[31]. This phase can be identified from the magnetic peak at 1.28 Å^{-1}. Unlike the common spinel counterparts [15,18], we find no structural transitions in Co_2VO_4 at all measured temperatures. Nonetheless, we observed an insignificant shrinking of the unit cell that appears to saturate at ≈ 65 K.

Magnetization measurements were performed on a pellet of mass 6.15 mg and carried out using a superconducting quantum interference device (Quantum Design MPMS) magnetometer for various applied magnetic fields in the range of 0.03–7 T and 2–350 K, performing both zero-field-cooled (ZFC) and field-cooled (FC) measurements. Neutron powder diffraction (NPD) was performed on a 2 g polycrystalline sample on the time-of-flight powder diffractometer POW-GEN [32] located at the Spallation Neutron Source at Oak Ridge National Laboratory. The measurements were carried out with neutrons of central wavelengths 1.333 and 3.731 Å. The sample was loaded in a vanadium can which was attached to the cold end of a cryostat to reach temperatures in the range $2 \leqslant T \leqslant 300$ K. NPD in applied magnetic fields was performed using E6 [33] and E9 [34] diffractometers at the BER II reactor at the Helmholtz-Zentrum Berlin. Powder sample amounting 3.5 g was dispersed in deuterated methanol-ethanol mixture, which freezes into an amorphous glass upon cooling, and thereby fixes the powder orientation while applying a magnetic field. The E6 diffractometer was used to perform the temperature scans ranging from 15 to 200 K with an applied magnetic field of 0.25 and 2 T with wavelength 2.44 Å , and the E9 diffractometer was used to perform temperature scans ranging from 50 to 250 K with an applied magnetic field of 0, 0.05, and 0.5 T with wavelength 1.81 Å following FC protocol. Refinements of the diffraction data were carried out using FULLPROF [35].

The EMU spectrometer [36] at the ISIS Neutron and muon source was used to perform zero applied field muon spin relaxation (ZF-μ^+SR) and longitudinal field muon spin relaxation (LF-μ^+SR) measurements where the applied magnetic field and muon spin are collinear on the polycrystalline sample. The polycrystalline Co_2VO_4 sample amounting to 2.5 g was placed in a titanium holder with a 24-mm-diameter window. Muons falling outside the sample window were stopped in a silver mask, giving a nonrelaxing background. Here, 100% spin-polarized muons are produced by the source, implanted in the sample, and their time evolution measured. The time evolution of muon polarization is given by $P_z(t)$. A normalized sample polarization immediately after muon implantation $P_s(0)$ was obtained after background correction. The ZF-μ^+SR scans were performed at various temperatures in the 10–250 K range. To elucidate dynamic aspects, LF-μ^+SR measurements were performed at 250, 125, 75, and 10 K with applied fields of 0.005, 0.05, 0.2, and 0.3 T. The data were analyzed using the muon analysis module of MANTID [37].

To understand the MR in Co_2VO_4, we carried out two sets of first-principles electronic structure calculations: (i) *delocalized* and (ii) *localized*. The delocalized calculations were performed using DFT in conjunction with the generalized gradient approximation (GGA) for exchange-correlation functional in all-electron projected augmented plane-wave formalism implemented in the Vienna *Ab initio* Simulation Package including spin-orbit coupling (SOC) [38,39]. We
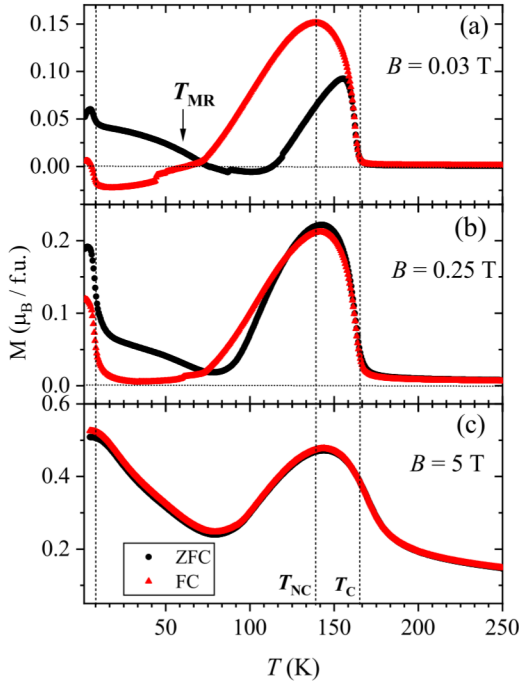
FIG. 1. Temperature dependence of zero-field-cooled (ZFC; black circle) and field-cooled (FC; red triangle) magnetization measurements performed for applied magnetic fields 0.03, 0.25, and 5 T. T_C and T_{NC} represent the transition temperatures to collinear and noncollinear magnetic structures, respectively, as explained in the text. Magnetization reversal temperature is represented by T_{MR} for $B = 0.03\,T$

used a plane-wave cutoff energy of 500 eV and $4 \times 4 \times 4$ **k**-mesh for the Brillouin zone integration. Structure optimization is performed by randomly replacing 50% V_B with Co_B in the bulk CoV_2O_4 structure that has the lowest total energy among all the considered configurations.

III. RESULTS AND DISCUSSIONS

Figure 1 shows the temperature (T) dependence of the ZFC and FC magnetization (M) of Co_2VO_4 at applied magnetic field $B = 0.03$, 0.25, and 5 T. Four features are identified for $B = 0.03\,T$. First, a sharp rise is observed at $T_C = 168(1)\,K$ ($C = $ collinear) corresponding to ferrimagnetic response and, second, with an onset of a decrease at $T_{NC} = 138(8)\,K$ ($NC = $ noncollinear), for both FC and ZFC. The third feature occurs at the temperature range $T_{MR} \sim 65$–$130\,K$, where the magnetization reverses, dependent on the cooling protocol (i.e., FC or ZFC). Here, T_{MR} can also be refereed to as compensation temperature [1,11]. Finally, <20 K, there is an upturn in magnetization, suggestive of a metamagnetic behavior, likely due to the $Co_3V_2O_8$ impurity phase [40]. MR does not occur for fields $> \sim 0.25\,T$, and eventually, the ZFC and FC curves overlap for fields >5 T, and the temperature dependence becomes reversible.

The magnetization at T_C for $B = 0.1\,T$ is $0.2\,\mu_B$/f.u. (not shown), which is lower than that of CoV_2O_4 [41]. A high spin configuration $S = \frac{3}{2}$ ($3\,\mu_B$) for Co_A^{2+} and $S = 1$ ($2\,\mu_B$) for

V_B^{3+} have been reported for CoV_2O_4 [18]. This indicates the reduced magnetization in Co_2VO_4 is due to antiparallel Co_A and Co_B/V_B (ferrimagnetic) assuming high spin configuration $S = \frac{3}{2}$, for Co^{2+} and $S = \frac{1}{2}$ for V_B, implying an oxidation state of 4+ for V. As discussed below, DFT calculations confirm the valence states of Co_B and V_B as well their magnetic ordering in the *localized solution*.

The NPD patterns for 140 and 25 K are presented in Figs. 2(a) and 2(b). Consistent with the aforementioned magnetic susceptibility, Fig. 3 shows the emergence of the (111) and (220) magnetic reflections at $T = 168(1)\,K$. At a lower temperature [$=138(2)\,K$], a weak (200) magnetic reflection is also observed [inset of Fig. 2(a)]. We emphasize that (200) is forbidden by $Fd\bar{3}m$. In the case of MnV_2O_4, observation of (200) is linked to spin canting of the spinel B site and a structural transition [15]. The temperature dependence of the three magnetic Bragg reflections is shown in Fig. 3. These curves are fitted to a power law function. The critical temperature obtained for reflections (111) and (220) is $T_C = 167.8 \pm 0.4\,K$ and for (200) at $T_{NC} = 138.5 \pm 7.5\,K$. We also note that the critical exponents associated with (111) and (200) are different, at 0.71 ± 0.02 and 0.5 ± 0.1, respectively.

To restrict the refinement of the neutron powder data, we exclude the irreducible basis vectors (BVs), on both the A and B sites, that are inconsistent with the strongest observed peaks in the powder diffraction pattern. These BVs are [for $Fd\bar{3}m$ and propagation vector $k = (0, 0, 0)$] found using BASIREPS [35] and SARAH [42]. We find that the simplest model consistent with both magnetization and powder diffraction data consists of BVs from the IR $\Gamma10$ with A- and B-sublattice moments arranged antiparallel. The magnetic representation in this case corresponds to Shubnikov space group $I4_1/am'd'$ (representation mGM4+) [43,44]. This picture is consistent with observations of other spinel vanadates [15,18] as well as recommendations made for magnetic interactions in Co_2VO_4 [8]. Table I lists $|F_{hkl}|^2$ for prominent magnetic reflections calculated using these BVs. Note that the intensity on (200) could be explained only by ψ_B^2 (AFM), while (220) has no contributions from ψ_B^1 (FM). As seen in Table I, FM order on the A site (ψ_A^1) gives rise to intensity in both the (220) and (111) reflections, while FM order on the B site (ψ_B^1) only gives rise to intensity on (111). The FM ordered moment on the A site can therefore be explicitly distinguished from that of the B site, and the relative magnitudes of the ordered moments can be directly extracted from the refinement. While the net ferrimagnetic moment can be directly deduced from NPD, it cannot distinguish individual contributions from Co_B and V_B. We note that combination of ψ_B^1 (c axis) and ψ_B^2 (ab pane) leads to the commonly observed two-in-two-out configuration in pyrochlore structures [15].

The refinements of NPD data at $B = 0\,T$ at the temperature range 5–250 K yield the sublattice magnetic moments as shown in Fig. 4(a). To compare sublattice magnetizations, we present the refined magnetic moments normalized to formula units. Refined moments on A and B sites are labeled as $\mu_{A(FM)}$, $\mu_{B(FM)}$, and $\mu_{B(AFM)}$, respectively. The total moment $\mu_{total} = \mu_{A(FM)} + \mu_{B(FM)}$ is shown in Fig. 4(b). Contributions from $\mu_{B(AFM)}$ (AFM, see Table I) cancel out and thus do not contribute to the total moment. As shown, μ_{total} as a function of temperature exhibits magnetic behavior that resembles the
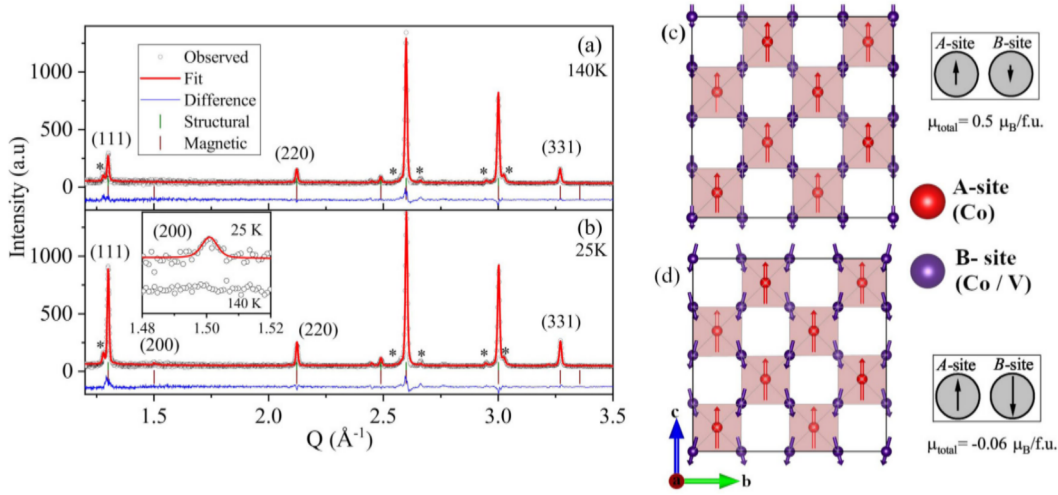
FIG. 2. Neutron diffraction patterns (NPD; black open circles), fits from the Rietveld refinement (red solid lines), and their differences (blue solid lines). The vertical bars are the expected Bragg peak positions as mentioned in the panels. The asterisks indicate impurity peaks. NPD observed (measured on POWGEN) (a) $T = 140$ K and (b) $T = 25$ K, corresponding to the data collected with center wavelengths 1.333 Å. In the inset of (b), one can see the emergence of (200) between 140 and 25 K. (c) Magnetic structure of Co_2VO_4 at 140 K. (d) Magnetic structure at 25 K. The A site is occupied by Co (red), whereas B site occupancy is shared between Co and V (purple).

magnetization shown in Fig. 1(a). The two sublattice magnetizations obtained at low temperature are similar, consistent with the B site [$Co^{2+}V^{4+}$] ground state electronic structure. Indeed Fig. 4(b) shows three identified temperatures in magnetization T_C, T_{NC}, and T_{MR}. Similar analysis of the diffraction patterns under magnetic field $B = 2$ T also yield distinguishable $\mu_{A(FM)}$ and $\mu_{B(FM)}$. However, μ_{total} at $B = 2$ T does not show MR (Fig. 5), as $\mu_{A(FM)}$ is always larger than $\mu_{B(FM)}$ for all temperatures, consistent with the observation >0.25 T (Fig. 1). It is not possible to extract $\mu_{B(AFM)}$ reliably in these measurements, as the defused signal from ethanol-methanol mixture overshadows the weak (200) peak.

To determine the possible dynamic origin of sublattice ordering, we employ polarized muon spectroscopy. The ZF-μ^+SR measurements were performed at various temperatures in the region 10–250 K. In the paramagnetic region ($T >$

T_C), the ZF-μ^+SR polarization spectra show temperature-independent relaxation with full polarization. This region is parameterized with static Kubo-Toyabe times exponential decay, accounting for nuclear and electronic moments [45]:

$$P_z(t) = P_{z_1}(0)\left[\exp\left(-\frac{\delta^2 t^2}{2}\right)(1 - \delta^2 t^2)\frac{2}{3} + \frac{1}{3}\right]$$
$$\times e^{-\lambda t} + P_{z_2}(0), \tag{1}$$

where P_{z_1} represents the polarization associated with the sample, and P_{z_2} is the nonrelaxing polarization from muons missing the sample, which could also include a nonrelaxed component present in the sample. Here, δ accounts for the relaxation rate due to the coupling of nuclear moments and muons and λ for the relaxation rate due to electron moments and muons coupling. At T_C, a sharp loss of the initial polarization is observed. This is typical for a magnetically
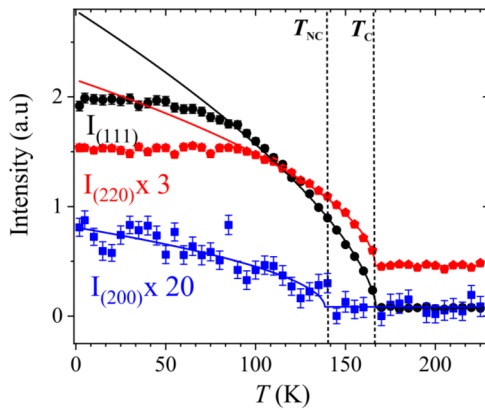

FIG. 3. Temperature dependencies of integrated intensities of the Bragg peak (111), (220), and (200) reflections for $B = 0$ T. The solid lines represent respective power law fits. T_C features can be identified from the ordering of (111) and (220) and T_{NC} from ordering of (200).

TABLE I. Magnetic structure factors computed are presented as $|F_{hkl}|^2$ (normalized) for the magnetic reflections (hkl) using basis vectors (BVs) of the irreducible representation (IR) belonging to A and B sites.

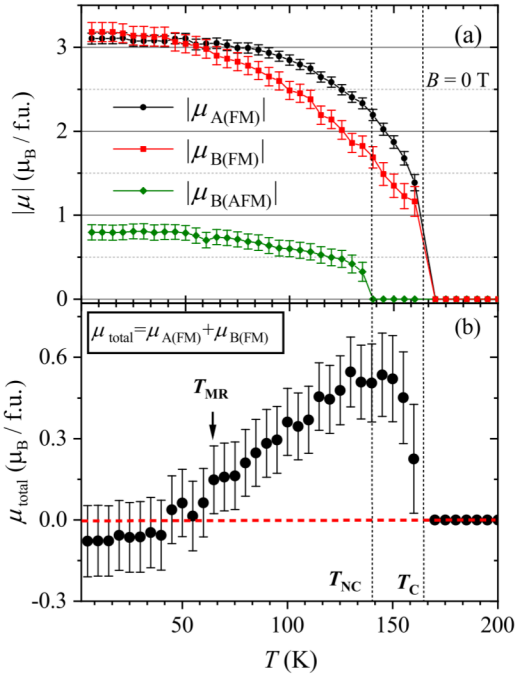| Site	IR		BVs	$\|F_{111}\|^2$	$\|F_{200}\|^2$	$\|F_{220}\|^2$	$\|F_{331}\|^2$
A site 8b	$\Gamma 10$	ψ_A^1 (FM)	(0 0 1) (0 0 1)	0.68	0	1.00	0.27
B site 16c	$\Gamma 10$	ψ_B^1 (FM)	(0 0 1) (0 0 1) (0 0 1) (0 0 1)	0.51	0	0	0.2
		ψ_B^2 (AFM)	(−1 −1 0) (1 1 0) (−1 1 0) (1 −1 0)	0.1	0.04	0.03	0.04

FIG. 4. (a) The magnitude of A- and B-sublattice moments obtained from Rietveld refinement for $B = 0$ T. (b) Total moment (per f.u.) calculated by adding ferromagnetic (FM) moments. Temperature dependence of total moment emulates the magnetization reversal as observed in magnetization measurement.

FIG. 5. (a) Magnitude of A- and B-sublattice moments obtained from Rietveld refinement for $B = 2$ T. (Inset) Total moment (per f.u.) calculated by adding moments along the c direction. Temperature dependence of total moment emulates magnetization for fields >0.25 T.

relaxation of the muon signal through this temperature region. Notably, there is no sharp peak in the relaxation rate at T_C, as one would expect for a typical magnetic phase transition. Fitting the low-temperature data ($T < 60$ K) with β as a free parameter shows β decreasing steadily, reaching a value ≈ 0.5 at 12 K. While we note that $\beta = 0.5$ could be a signature to glassy transition [46], typical for an inverse spinel at low temperatures [28,47], the $Co_3V_2O_8$ impurity phase is also

ordered system, where the missing polarization is associated with strong electronic moments, giving rise to an unresolved precession signal owing to the finite muon pulse width at the source (ISIS). Below T_C, a one-component stretched exponential decay function is sufficient to parametrize the ordered region, i.e.,

$$P_z(t) = P_{z_1}(0) \exp[-(\lambda t)^\beta] + P_{z_2}(0). \quad (2)$$

In Eq. (2), P_{z_1} represents the polarization associated with the sample, and P_{z_2} is the nonrelaxing polarization from muons missing the sample, which could also include a nonrelaxed component present in the sample. Here, λ is the relaxation rate and β the stretching exponent. When $\beta = 1$, Eq. (2) turns into simple exponential decay. We find that, above T_{MR}, the best fit to the data is obtained with β fixed at 1. However, below T_{MR}, acceptable fits could only be obtained fitting β as a free parameter.

Figure 6 shows the normalized sample polarization when muons are stopped in the sample ($t = 0$) and $P_s(0)$ and relaxation rate λ are extracted from ZF-μ^+SR data as a function of temperature. Below T_C, $P_s(0)$ is reduced to $\frac{1}{3}$ of its initial value ($T > T_C$). Intriguingly, there is a further loss of polarization as the temperature is reduced below T_C, reaching a minimum at T_{NC} and only regaining the $\frac{1}{3}$ value of the initial polarization at T_{MR}. The broad dip between T_C and T_{MR} suggests that muons are experiencing changes in the magnetic structure right through the region. This is consistent with the corresponding peak in the relaxation rate, suggesting a spin fluctuation/reorientation process is driving an enhanced T_1
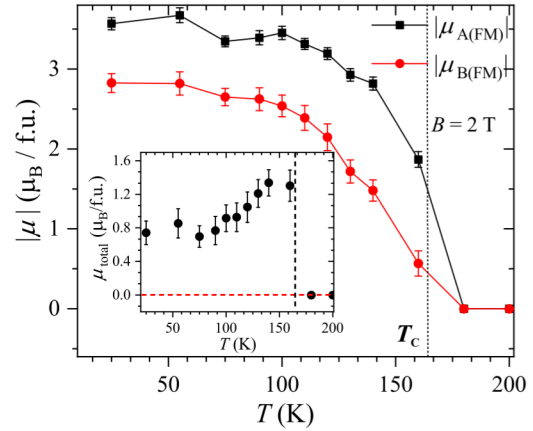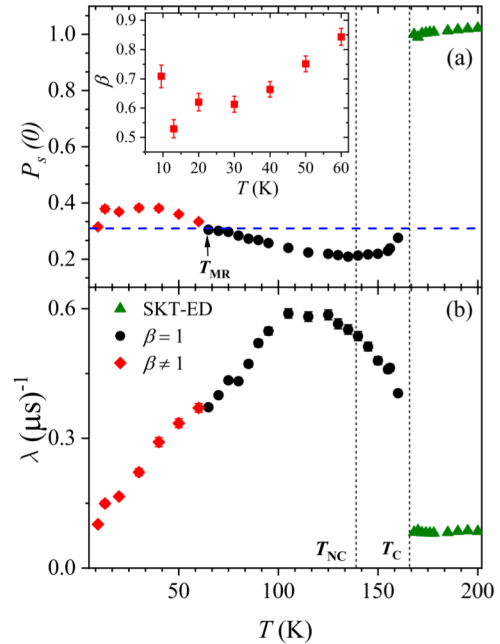

FIG. 6. (a) Initial polarization and (b) relaxation rate extracted from fits to the zero applied field muon spin relaxation (ZF-μ^+SR) polarization spectra. For $T < T_C$, fits are to Eq. (2), with β as a free parameter below T_{MR} (red points). Above T_C, fits are carried out to Eq. (1) (green points). Inset of (a) β vs T, where β reaches 0.5 at 12 K.
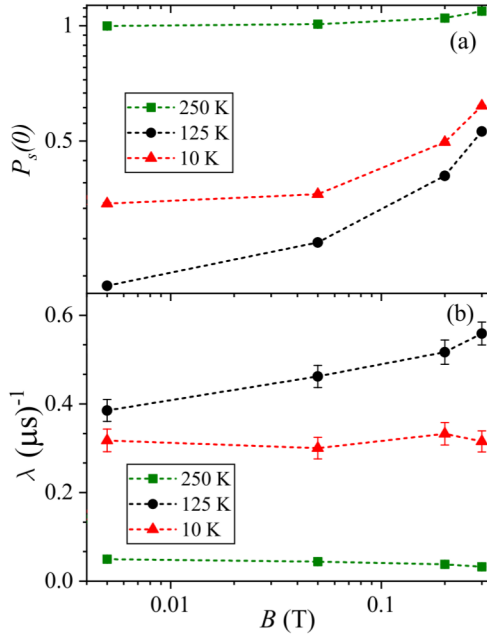
FIG. 7. (a) Initial polarization and (b) relaxation rate extracted from fits to the longitudinal field muon spin relaxation (LF-μ^+SR) polarization spectra with Eq. (2). At 125 K, complete decoupling was realized with a tiny field of 0.005 T. Due to instrument effects, $P_s(0)$ goes beyond 1 for higher fields.

likely to contribute to the measured behavior. Further work is needed to properly understand the low-temperature muon response.

Initial polarization and relaxation measurements for LF-μ^+SR up to 0.3 T were carried out at 10, 125, and 250 K. Values obtained for $P_s(0)$ and λ obtained from fitting the data to Eq. (2) with β fixed at 1 are shown in Fig. 7, with T_1 spin relaxation λ persisting at all temperatures to the highest fields measured. This suggests that spin dynamics are present at all temperatures, both in the paramagnetic regime above T_C and also in the ordered state. We note that the strongest relaxation is measured at 125 K, close to T_{MR}, a region where electron delocalization is predicted by DFT, and at this temperature, the relaxation rate [Fig. 7(b)] appears to increase with the applied field in contrast to results measured at 10 K. A clear recovery of the initial polarization is seen at the highest fields measured, although full decoupling is not achieved, with only 50% of the polarization being recovered. We suggest this is the result of both large internal fields and spin dynamics below T_C in this material.

To supplement the experimental results, we conduct *delocalized* and *localized* electronic structure calculations. For the delocalized calculations, we employ standard DFT with a GGA functional. In the localized calculations, we add the onsite electron correlation following the scheme of Dudarev *et al.* [48], in which only the effective value of onsite correlation ($U_{eff} = U - J = 4.5$ eV for $3d$ electrons of Co and V [49]) is meaningful. To be on equal footing, we also perform another calculation using the same value of U_{eff} and find the delocalized solution, which has higher total energy than in the

localized solution. As expected, the net magnetic moments do not change significantly with the use of U_{eff} in the delocalized results.

As shown below, the *localized* calculations are akin to the low-temperature ground state, whereas the *delocalized* ones correspond to the high-temperature ferrimagnetic phase. Both *localized* and *delocalized* calculations show similar magnetic moments for Co_A, while they are drastically different for Co_B and V_B. These changes in the local magnetic moments are consistent with the low-temperature neutron diffraction results (Table II). The major contribution to the net magnetic moment is from spin (Table II), while the orbital contributions are small, and slight fluctuations for Co_B are found (not shown). In the localized solution, we find canted spin structures for Co_B and V_B in qualitative agreement with the experimental results at 25 K (Table II). A notable prediction is the AFM alignment of Co_A moments with respect to Co_B with a small canting in the planar direction (Table II). For Co_A, the canting is not resolved experimentally. At the B site, the V_B moments follow the Co_B moments. These are remarkable changes in the frustrated magnetic structures of the well-known spinel vanadates, viz., FeV_2O_4 [16] and MnV_2O_4 [15], in which V_B moments are two-in-two-out as observed experimentally. The calculated net magnetic moment parallel to the c direction is negative, in agreement with the low-temperature data. The discrepancy between theory and experiment in the magnitude of net magnetic moment is likely due to the choice of atomic sphere sizes used in the calculations, i.e., Co_A moment $\sim 2.6\,\mu_B$ is smaller than the experiment $3.07\,\mu_B$. We find $3d$ Co/V and O($2p$) hybridization, which we argue may affect the magnetic moments on both Co and V. In calculations, the canting is small, which results in a large magnetic moment ($\sim 3.7\,\mu_B$) along the z direction, which qualitatively agrees with the experiment (see Table II). Another possibility for the slight discrepancy is random occupancy of Co and V in the B sites.

Interestingly, the magnetic moments obtained with the delocalized solutions agree with the higher temperature data, indicating a more itinerant scenario [50]. The magnetic moments on the B site are sensitive to the choice of U_{eff} (i.e., localized or delocalized), while the moments on the A site remain relatively unchanged. Interatomic charge transfer from Co_B to V_B sites reduces the effective Co_B moments. This delicate balance between Co_A, Co_B, and V_B magnetic moments in the localized and delocalized limits presumably leads to the MR.

To demonstrate that the electronic configuration of Co is $3d^7$ (i.e., Co^{2+}) and that of V_B is $3d^1$ (i.e., V^{4+}), we examine the partial density of states (PDOS) of each atom in the localized calculations. Figure 8 shows very well split-off $e_g \downarrow$ and $t_g \uparrow$ $3d$ states of Co_A around the Fermi level due to the tetrahedral crystal field of oxygen atoms. In Co_B and V_B, the splittings of the threefold t_{2g} states are less obvious. Because of the distorted octahedral crystal field effect [22], these states split into an a_{1g} and doubly degenerate e'_g, resulting in $3d^7$, $S = \frac{3}{2}$ (occupying $e'_g \uparrow$) for Co_B^{2+} as in Co_A^{2+}, and $3d^1$, $S = \frac{3}{2}$ (occupying a_{1g}) for V_B^{4+} in the localized limit as inferred from the current and earlier experiments [8]. An interesting change is in the vanadium oxidation state from $V^{3+}(3d^2)$, which is common in the standard spinel compounds, to $V^{4+}(3d^1)$

TABLE II. Canted magnetic moment components (spin + orbital) (μ_x, μ_y, μ_z) of individual atom and total magnetic moments (μ_{total}) (per f.u.) in units of μ_B in Co_2VO_4 obtained from Rietveld refinement from zero field data and theory (GGA + SOC and GGA + SOC + U calculations). For oxygens, only the calculated moments are given.

		Experiment		Theory	
Site	Atom	140 K	25 K	GGA + SOC	GGA + U + SOC
A site	Co_A	$(0, 0, 2.18(6))$	$(0, 0, 3.07(6))$	$(0, 0, 2.48)$	$(0.80, 0, 2.74)$
B site	Co_B	NA	NA	$(0, 0, -0.43)$	$(-0.81, \|0.13\|, -2.72)$
	V_B	NA	NA	$(0, 0, -1.29)$	$(-0.34, \|0.02\|, -1.02)$
	$Co_B + V_B$	$(0, 0, -1.68(2))$	$(\|0.88(8)\|, \|0.88(8)\|, -3.13(1))$	$(0, 0, -1.72)$	$(-1.15, \|0.15\|, -3.74)$
X site	O	NA	NA	$(0, 0, 0.09)$	$(0, 0, 0.02)$
μ_{total} (μ_B/f.u.)		$(0, 0, 0.50(8))$	$(0, 0, -0.06(7))$	$(0, 0, 1.14)$	$(-0.32, 0, -0.90)$

with $S = \frac{1}{2}$, consistent with the magnetic moment [8] at low temperature. We note that Co_B^{2+} and V_B^{4+} moments change significantly in the delocalized solutions (Table II), which corresponds to high temperatures. Specifically, the magnetic moment on the Co_B is significantly reduced, suggesting a fluctuation of magnetic moment of Co_B between a low spin state Co^{3+} ($S = 0$) and a high spin state Co^{2+} ($S = \frac{3}{2}$). On the other hand, it is the opposite for V_B. This is expected because itinerant electrons can hop easily from Co_B to V_B due to a narrow splitting of t_{2g} states in both atoms. These results suggest that the inverse spinel undergoes charge fluctuations $[Co^{2+}][Co^{(2+\delta)+}V^{(4-\delta)+}]O_4$, where $\delta < 1$ above T_{MR}.

The T_1 relaxation observed with μ^+SR supplements the theoretical suggestion that the B-site ions undergo charge delocalization-to-localization crossover. A similar delocal-

FIG. 8. Spin-resolved partial density of states (PDOS) of Co_A, Co_B, and V_B. The positive and negative values indicate PDOS of majority and minority spin electrons, respectively. The spins of Co_A are aligned antiferromagnetically with respect to Co_B and V_B. Both Co at A and B sites have $3d^7$ valence electrons, indicating the formation of a Co^{2+} ion. The distorted octahedral crystal field splits t_{2g} into a_{1g} and doubly degenerate e_g states at site B. For Co_B, two electrons occupy the lower e_g states forming a $S = \frac{3}{2}$ state, while for V_B, one electron occupies a_{1g}, yielding V^{4+} oxidation state with $S = \frac{1}{2}$.

ization mechanism was suggested by Belov [11] in inverse spinel magnetite Fe_3O_4 employing a so-called magneto-electronic sublattice model. Fe_3O_4 is well known for its metal-insulator transition or Verwey transition [51]. Belov [11,12] proposed an electronic hopping or delocalization on the B site creating the magneto-electronic sublattice with its magnetization antiparallel to that of the two combined sublattices, leading to a decreased spontaneous magnetization. Below T_{MR} in Co_2VO_4, the delocalized electrons would gradually localize, leading to $[Co^{2+}][Co^{(2+\delta)+}V^{(4-\delta)+}]O_4 \Rightarrow [Co^{2+}][Co^{2+}V^{4+}]O_4$ (where $\delta < 1$) and thus decreasing spontaneous magnetization $<0\,\mu_B$/f.u. This is consistent with the near-perfect compensation of the two sublattice magnetizations, coexisting with an AFM ordering of the V^{+4} moments.

IV. CONCLUSIONS

Our interest in inverse cobalt vanadium spinel springs from the highly unconventional temperature-dependent magnetization of the compound, where a spontaneous MR takes place. We have performed magnetization measurements and revealed at least three distinct anomalies. NPD analysis reveals two antiparallel magnetic structures, each belonging to magnetic ions on A and B sites. The relative balance of these two structural components in essence determines the net magnetic moment in the unit cell. However, the order parameter on one site develops more moderately than that on the other site. While in itself unusual, a tipping of the magnetic balance, caused by such site-specific magnetic fluctuation, gives rise to a spontaneous flipping of the magnetization as the temperature is lowered. The MR determined at zero field is sensitive to an applied magnetic field, such that, above $B \sim 0.25$ T, instead of a reversal, a minimum in the magnetization is apparent at T_{MR}.

The root cause of this site specificity is unveiled by DFT results. The DFT calculations were performed assuming delocalized and localized electrons. We argue that the MR is a consequence of the itineracy of Co and V electrons in the B site. The *delocalized* calculations, which we associate with the behavior of the high temperature of the system (around T_C), predict relatively small net magnetic moments on the B site compared with the A site, giving rise to the net ferrimagnetic moment observed near T_C. The DFT calculations also show that the Co moments on the A site are less sensitive to temperature change with electronic configuration $Co^{2+}(3d^7)$
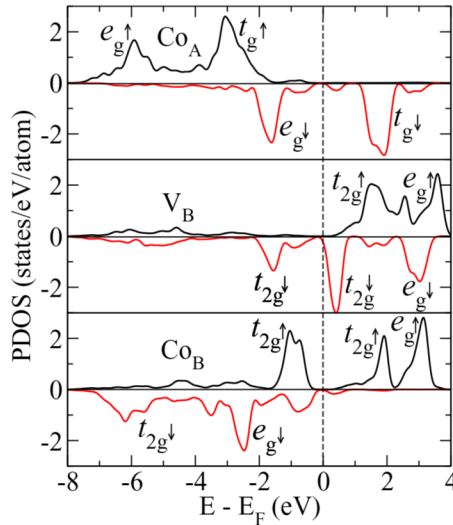
with $S = \frac{3}{2}$. For the B site, the DFT calulations find mixed oxidation states for Co and V that at low temperatures tend toward their localized values, namely, Co^{2+} ($S = \frac{3}{2}$) (as in the A site) and V^{4+} ($S = \frac{1}{2}$). This suggests that the MR is likely driven by *delocalized*-to-localized crossover of the 3d electrons of the Co/V atoms in the B site. We note that quantitative disagreements between theory and experiment are expected owing to the complexities of this inverse spinel Co_2VO_4 and the random distribution of Co and V in the B site. Polarized muon spectroscopy as a function of temperature is consistent with the neutron diffraction and magnetization results but adds insights that have been predicted by our DFT calculations. It shows that highly delocalized-fluctuating magnetic moments at high temperatures gradually tend to localize at lower temperatures, in agreement with our DFT calculations.

ACKNOWLEDGMENTS

[1] L. Néel, Propriétés magnétiques des ferrites; ferrimagnétisme et antiferromagnétisme, Ann. Phys. **12**, 137 (1948).

[2] Y. Yafet and C. Kittel, Antiferromagnetic arrangements in ferrites, Phys. Rev. **87**, 290 (1952).

[3] V. Tsurkan, H.-A. Krug von Nidda, J. Deisenhofer, P. Lunkenheimer, and A. Loidl, On the complexity of spinels: magnetic, electronic, and polar ground states, Phys. Rep. **926**, 1 (2021).

[4] Y. Yamasaki, S. Miyasaka, Y. Kaneko, J.-P. He, T. Arima, and Y. Tokura, Magnetic Reversal of the Ferroelectric Polarization in a Multiferroic Spinel Oxide, Phys. Rev. Lett. **96**, 207204 (2006).

[5] A. Ruff, Z. Wang, S. Zherlitsyn, J. Wosnitza, S. Krohns, H.-A. Krug von Nidda, P. Lunkenheimer, V. Tsurkan, and A. Loidl, Multiferroic spin-superfluid and spin-supersolid phases in $MnCr_2S_4$, Phys. Rev. B **100**, 014404 (2019).

[6] L. Balents, Spin liquids in frustrated magnets, Nature (London) **464**, 199 (2010).

[7] D. Bergman, J. Alicea, E. Gull, S. Trebst, and L. Balents, Order-by-disorder and spiral spin-liquid in frustrated diamond-lattice antiferromagnets, Nat. Phys. **3**, 487 (2007).

[8] N. Menyuk, K. Dwight, and D. G. Wickham, Magnetization Reversal and Asymmetry in Cobalt Vanadate (IV), Phys. Rev. Lett. **4**, 119 (1960).

[9] A. Kumar and S. Yusuf, The phenomenon of negative magnetization and its implications, Phys. Rep. **556**, 1 (2015).

[10] D. T. Adroja, S. Sharma, C. Ritter, A. D. Hillier, D. Le, C. V. Tomy, R. Singh, R. I. Smith, M. Koza, A. Sundaresan, and S. Langridge, Muon spin rotation and neutron scattering investigations of the B-site ordered double perovskite Sr_2DyRuO_6, Phys. Rev. B **101**, 094413 (2020).

[11] K. P. Belov, Ferrimagnets with a 'weak' magnetic sublattice, Usp. Fiz. Nauk [Sov. Phys. Usp.] **39**, 623 (1996).

[12] K. P. Belov, Electronic processes in magnetite (or, "Enigmas of magnetite"), Usp. Fiz. Nauk [Sov. Phys. Usp.] **36**, 380 (1993).

[13] S. Niitaka, H. Ohsumi, K. Sugimoto, S. Lee, Y. Oshima, K. Kato, D. Hashizume, T. Arima, M. Takata, and H. Takagi, A-Type Antiferro-Orbital Ordering with $I4_1/a$ Symmetry and Geometrical Frustration in the Spinel Vanadate MgV_2O_4, Phys. Rev. Lett. **111**, 267201 (2013).

[14] S.-H. Lee, D. Louca, H. Ueda, S. Park, T. J. Sato, M. Isobe, Y. Ueda, S. Rosenkranz, P. Zschack, J. Íñiguez, Y. Qiu, and R. Osborn, Orbital and Spin Chains in CoV_2O_4, Phys. Rev. Lett. **93**, 156407 (2004).

[15] V. O. Garlea, R. Jin, D. Mandrus, B. Roessli, Q. Huang, M. Miller, A. J. Schultz, and S. E. Nagler, Magnetic and Orbital Ordering in the Spinel MnV_2O_4, Phys. Rev. Lett. **100**, 066404 (2008).

[16] G. J. MacDougall, V. O. Garlea, A. A. Aczel, H. D. Zhou, and S. E. Nagler, Magnetic order and ice rules in the multiferroic spinel FeV_2O_4, Phys. Rev. B **86**, 060414(R) (2012).

[17] Q. Zhang, M. Ramazanoglu, S. Chi, Y. Liu, T. A. Lograsso, and D. Vaknin, Magnetic excitations and anomalous spin-wave broadening in multiferroic FeV_2O_4, Phys. Rev. B **89**, 224416 (2014).

[18] H. Ishibashi, S. Shimono, K. Tomiyasu, S. Lee, S. Kawaguchi, H. Iwane, H. Nakao, S. Torii, T. Kamiyama, and Y. Kubota, Small crystal distortion and long-range antiferro-orbital ordering in the spinel oxide CoV_2O_4, Phys. Rev. B **96**, 144424 (2017).

[19] Y. Nii, H. Sagayama, T. Arima, S. Aoyagi, R. Sakai, S. Maki, E. Nishibori, H. Sawa, K. Sugimoto, H. Ohsumi, and M. Takata, Orbital structures in spinel vanadates AV_2O_4(A = Fe, Mn), Phys. Rev. B **86**, 125142 (2012).

[20] R. Koborinai, S. E. Dissanayake, M. Reehuis, M. Matsuda, T. Kajita, H. Kuwahara, S.-H. Lee, and T. Katsufuji, Orbital Glass State of the Nearly Metallic Spinel Cobalt Vanadate, Phys. Rev. Lett. **116**, 037201 (2016).

[21] D. Reig-i-Plessis, D. Casavant, V. O. Garlea, A. A. Aczel, M. Feygenson, J. Neuefeind, H. D. Zhou, S. E. Nagler, and G. J.

MacDougall, Structural transition and orbital glass physics in near-itinerant CoV_2O_4, Phys. Rev. B **93**, 014437 (2016).

[22] A. Kismarahardja, J. S. Brooks, A. Kiswandhi, K. Matsubayashi, R. Yamanaka, Y. Uwatoko, J. Whalen, T. Siegrist, and H. D. Zhou, $Co[V]_2O_4$: A Spinel Approaching the Itinerant Electron Limit, Phys. Rev. Lett. **106**, 056602 (2011).

[23] D. B. Rogers, R. J. Arnott, A. Wold, and J. B. Goodenough, The preparation and properties of some vanadium spinels, J. Phys. Chem. Solids **24**, 347 (1963).

[24] C. Mu, J. Mao, J. Guo, Q. Guo, Z. Li, W. Qin, Z. Hu, K. Davey, T. Ling, and S.-Z. Qiao, Rational design of spinel cobalt vanadate oxide Co_2VO_4 for superior electrocatalysis, Adv. Mater. **32**, 1907168 (2020).

[25] D. G. Wickham and J. B. Goodenough, Suggestion concerning magnetic interactions in spinels, Phys. Rev. **115**, 1156 (1959).

[26] N. Sakamoto, Magnetic properties of cobalt titanate, J. Phys. Soc. Jpn. **17**, 99 (1962).

[27] S. Thota, M. Reehuis, A. Maljuk, A. Hoser, J.-U. Hoffmann, B. Weise, A. Waske, M. Krautz, D. C. Joshi, S. Nayak, S. Ghosh, P. Suresh, K. Dasari, S. Wurmehl, O. Prokhnenko, and B. Büchner, Neutron diffraction study of the inverse spinels Co_2TiO_4 and Co_2SnO_4, Phys. Rev. B **96**, 144104 (2017).

[28] S. Nayak, S. Thota, D. C. Joshi, M. Krautz, A. Waske, A. Behler, J. Eckert, T. Sarkar, M. S. Andersson, R. Mathieu, V. Narang, and M. S. Seehra, Magnetic compensation, field-dependent magnetization reversal, and complex magnetic ordering in Co_2TiO_4, Phys. Rev. B **92**, 214434 (2015).

[29] V. W. Rüdorff, G. Walter, and H. Becker, Über einige Ox-overbindungen und Doppeloxyde des vierwertigen Vanadins, Z. Anorg. Allg. Chem. **285**, 287 (1956).

[30] N. Qureshi, M. Zbiri, J. Rodríguez-Carvajal, A. Stunault, E. Ressouche, T. C. Hansen, M. T. Fernández-Díaz, M. R. Johnson, H. Fuess, H. Ehrenberg, Y. Sakurai, M. Itou, B. Gillon, T. Wolf, J. A. Rodríguez-Velamazan, and J. Sánchez-Montero, Experimental magnetic form factors in $Co_3V_2O_8$: a combined study of *ab initio* calculations, magnetic Compton scattering, and polarized neutron diffraction, Phys. Rev. B **79**, 094417 (2009).

[31] W. Jauch, M. Reehuis, H. J. Bleif, F. Kubanek, and P. Pattison, Crystallographic symmetry and magnetic structure of CoO, Phys. Rev. B **64**, 052102 (2001).

[32] A. Huq, J. P. Hodges, O. Gourdon, and L. Heroux, Powgen: A third-generation high-resolution high-throughput powder diffraction instrument at the spallation neutron source, Z. Kristallogr. Proc. **1**, 127 (2011).

[33] A. Buchsteiner and N. Stüßer, Optimizations in angular dispersive neutron powder diffraction using divergent beam geometries, Nucl. Instrum. Methods Phys. Res., Sect. A **598**, 534 (2009).

[34] A. Franz and A. Hoser, E9: The fine resolution powder diffractometer (FIREPOD) at BER II, J. Large-Scale Res. Facil. **3**, A103 (2017).

[35] J. Rodríguez-Carvajal, Recent advances in magnetic structure determination by neutron powder diffraction, Phys. B: Condens. Matter **192**, 55 (1993).

[36] S. R. Giblin, S. P. Cottrell, P. J. C. King, S. Tomlinson, S. J. S. Jago, L. J. Randall, M. J. Roberts, J. Norris, S. Howarth, Q. B.

Mutamba, N. J. Rhodes, and F. A. Akeroyd, Optimising a muon spectrometer for measurements at the ISIS pulsed muon source, Nucl. Instrum. Methods Phys. Res., Sect. A **751**, 70 (2014).

[37] O. Arnold, J. Bilheux, J. Borreguero, A. Buts, S. Campbell, L. Chapon, M. Doucet, N. Draper, R. Ferraz Leal, M. Gigg, V. Lynch, A. Markvardsen, D. Mikkelson, R. Mikkelson, R. Miller, K. Palmen, P. Parker, G. Passos, T. Perring, P. Peterson *et al.*, Mantid-data analysis and visualization package for neutron scattering and μSR experiments, Nucl. Instrum. Methods Phys. Res., Sect. A **764**, 156 (2014).

[38] G. Kresse and J. Furthmüller, Efficient iterative schemes for *ab initio* total-energy calculations using a plane-wave basis set, Phys. Rev. B **54**, 11169 (1996).

[39] G. Kresse and D. Joubert, From ultrasoft pseudopotentials to the projector augmented-wave method, Phys. Rev. B **59**, 1758 (1999).

[40] Y. Yasui, Y. Kobayashi, M. Soda, T. Moyoshi, M. Sato, N. Igawa, and K. Kakurai, Successive magnetic transitions of the kagomé staircase compound $Co_3V_2O_8$ studied in various magnetic fields, J. Phys. Soc. Jpn. **76**, 034706 (2007).

[41] Y. Huang, Z. Yang, and Y. Zhang, Magnetic, structural, and thermal properties of CoV_2O_4, J. Phys.: Condens. Matter **24**, 056003 (2012).

[42] A. S. Wills, A new protocol for the determination of magnetic structures using simulated annealing and representational analysis (SARAh), Phys. B (Amsterdam, Neth.) **276-278**, 680 (2000).

[43] J. Perez-Mato, S. Gallego, E. Tasci, L. Elcoro, G. de la Flor, and M. Aroyo, Symmetry-based computational tools for magnetic crystallography, Annu. Rev. Mater. Res. **45**, 217 (2015).

[44] H. T. Stokes, D. M. Hatch, and B. J. Campbell, ISOTROPY software suite, https://iso.byu.edu/

[45] R. Kubo and T. Toyabe, *Magnetic Resonance and Relaxation* (North Holland, Amsterdam, 1967), Vol. 29, p. 59.

[46] I. A. Campbell, A. Amato, F. N. Gygax, D. Herlach, A. Schenck, R. Cywinski, and S. H. Kilcoyne, Dynamics in Canonical Spin Glasses Observed by Muon Spin Depolarization, Phys. Rev. Lett. **72**, 1291 (1994).

[47] S. Thota and M. S. Seehra, Co-existence of ferrimagnetism and spin-glass state in the spinel Co_2SnO_4, J. Appl. Phys. **113**, 203905 (2013).

[48] S. L. Dudarev, G. A. Botton, S. Y. Savrasov, C. J. Humphreys, and A. P. Sutton, Electron-energy-loss spectra and the structural stability of nickel oxide: an LSDA $+ U$ study, Phys. Rev. B **57**, 1505 (1998).

[49] J. H. Lee, J. Ma, S. E. Hahn, H. B. Cao, M. Lee, T. Hong, H.-J. Lee, M. S. Yeom, S. Okamoto, H. D. Zhou, M. Matsuda, and R. S. Fishman, Magnetic frustration driven by itinerancy in spinel CoV_2O_4, Sci. Rep. **7**, 17129 (2017).

[50] C. Bhandari, M. E. Flatté, and D. Paudyal, Enhanced magnetic anisotropy in lanthanum M-type hexaferrites by quantum-confined charge transfer, Phys. Rev. Materials **5**, 094415 (2021).

[51] E. Verwey and P. Haayman, Electronic conductivity and transition point of magnetite ("Fe_3O_4"), Physica **8**, 979 (1941).